Supplementary Information

3-D-geometry-triggered transition from monotonic to nonmonotonic effects of wettability on multiphase displacements in homogeneous porous media

Wenhai Lei[1,2], Wenbo Gong[3], Xukang Lu[1], Yuankai Yang[4], Haien Yang[5], Moran Wang[1*]

[1]*Department of Engineering Mechanics and ASP, Tsinghua University, Beijing 100084, China*

[2]*Department of Engineering Mechanics, KTH Royal Institute of Technology, Stockholm 100 44, Sweden*

[3]*College of Safety and Ocean Engineering, China University of Petroleum, Beijing, China*

[4]*Institute of Fusion Energy and Nuclear Waste Management (IFN-2) - Nuclear Waste Management, Forschungszentrum Jülich GmbH, Julich 52425, Germany*

[5]*Xi'an Changqing Chemical Industry Group Co., Ltd., Xi'an 710021, China*

* Corresponding author. E-mail: moralwang@jhu.edu

Text S1: Microfluidic visualization system and 2.5D microfluidic chips

A microfluidic visualization platform was meticulously designed for conducting multiphase displacement experiments, as illustrated in Figure S1(a). The experimental setup consists of three integral components: a microfluidic porous media, a microscope imaging system, and an injection system. The microscope imaging system is equipped with a stereo fluorescence microscope (Nikon, SMZ18) and a CMOS camera (Nikon, DS-Ri2), enabling the capture of comprehensive images across the entire microfluidic porous media domain. The spatial resolution is 1.92 μm/pixel, and the time resolution is 1 s. The injection system integrates a microfluidic pressure controller (Fluigent, MFCS-EZ), a flow rate sensor (Fluigent, M), and three reservoirs, providing a higher resolution of flow rate compared to a syringe pump. The microfluidic chip is fixed by a homemade holder to connect the microfluidic chip to the injection system.

Based on the designed porous geometry, the pattern was intricately transferred onto a silicon wafer using micro-fabrication techniques, which involved standard photolithography and inductively coupled plasma-deep reactive ion etching. The 2D microfluidic porous geometry was generated using a random generation method to faithfully reproduce the statistical information inherent in natural rock samples (3D engineering porous media). Unlike traditional uniform-depth microfluidic porous media, which typically exhibit strong depth confinement, our approach involved combining sequential photolithography, multi-step etching methods, and an on-chip random generation algorithm. This innovative method introduced depth variation in the 2.5D microfluidic porous media, enabling the etching of larger pores to greater depths than smaller pores, as depicted in Figure S1(b).

For detailed 2.5D microfluidic chip fabrication methods, please refer to our previous work (*Lei et al.*, 2023; *Lei et al.*, 2024). Here we briefly introduce the fabrication method. The sequential photolithography and multi-etching processes are combined for fabricating silicon-based multi-depth microfluidic chips. Among these processing steps, mask design is the crucial soul. First, a high-resolution 2D porous structure pattern, aiming for a target pore size distribution resembling natural 3D porous media, is generated using a random generation algorithm known as the Quartet Structure Generation Set (QSGS) (*Lei et al.*, 2020; *Wang et al.*, 2007). To simplify the microfabrication processes, the target depth of each etched pattern is configured to be the same value. Here, this value can be chosen as the characteristic diameter of the desired pore size distribution (40 μm). Therefore, the depth value of pores in the microfluidic chips can be 40 μm, 80 μm, or 120 μm.

We utilized the maximal ball algorithm (*Blunt*, 2017) to identify the 2D width distribution of the porous structure. Statistical information about the width distributions can be acquired by calculating the ratios of these pore areas. Considering the impact of depth confinement on the hydraulic diameters distribution, we divided the aforementioned 2D diameter-labeled regions into three categories: the 1^{st}-depth region, the 2^{nd}-depth region, and the 3^{rd}-depth region. To achieve depth variations in pores and ensure mismatch tolerance during the fabrication, we designed the etching range to shrink to the inside of the pores with the etching times increase. As a result, the first mask for the 1^{st} etching is the original 2-D image containing the all-depth region, the second mask for the 2^{nd} etching is extracted from the first mask that contains the 2^{nd}-depth and 3^{rd}-depth regions, the third mask for the 3^{rd} etching is extracted from the second mask that only contains the 3^{rd}-depth region. Subsequently, the corresponding 2D geometry can be categorized into different depth regions, enabling the fabrication of depth-variable microfluidic chips (2.5D porous media) through sequential photolithography and multi-etching methods.

Based on the obtained pattern, the porous structures were created from a silicon wafer using micro-fabrication techniques, including multiple uses of standard photography, and inductively coupled plasma-deep reactive ion etching (ICP-DRIE). With an increase in etching cycles, the geometric confinement in the depth direction is gradually weakened. To get equal wettability on all surfaces within the microfluidic chip, all etched silicon wafers underwent a one-hour heating process at 1000°C in the presence of oxygen to create a uniform 100 nm silicon dioxide layer via thermal oxidation (*Chomsurin and Werth*, 2003). Finally, a Schott Borofloat 270 glass wafer with inlet and outlet ports was anodically bonded to the above thermally oxidized silicon.

For the water-air pair, water was dyed with fluorescein sodium salt (Macklin) at 100 ppm, and for the water-decane pair, oil was dyed with Nile red (Macklin) at 100 ppm. Invasion morphology images were recorded until the invading fluid reached the outlet. To ensure the cleanliness of all microfluidic porous media, a thorough cleaning process was implemented involving 50 pore volumes (PV) of acetone, followed by 50 PV of alcohol, 50 PV of HCl solution (4 vol.%), and finally 50 PV of DI water, sequentially. Finally, the cleaned media were dried using a stream of N_2 and subjected to a 12-hour vacuum treatment.

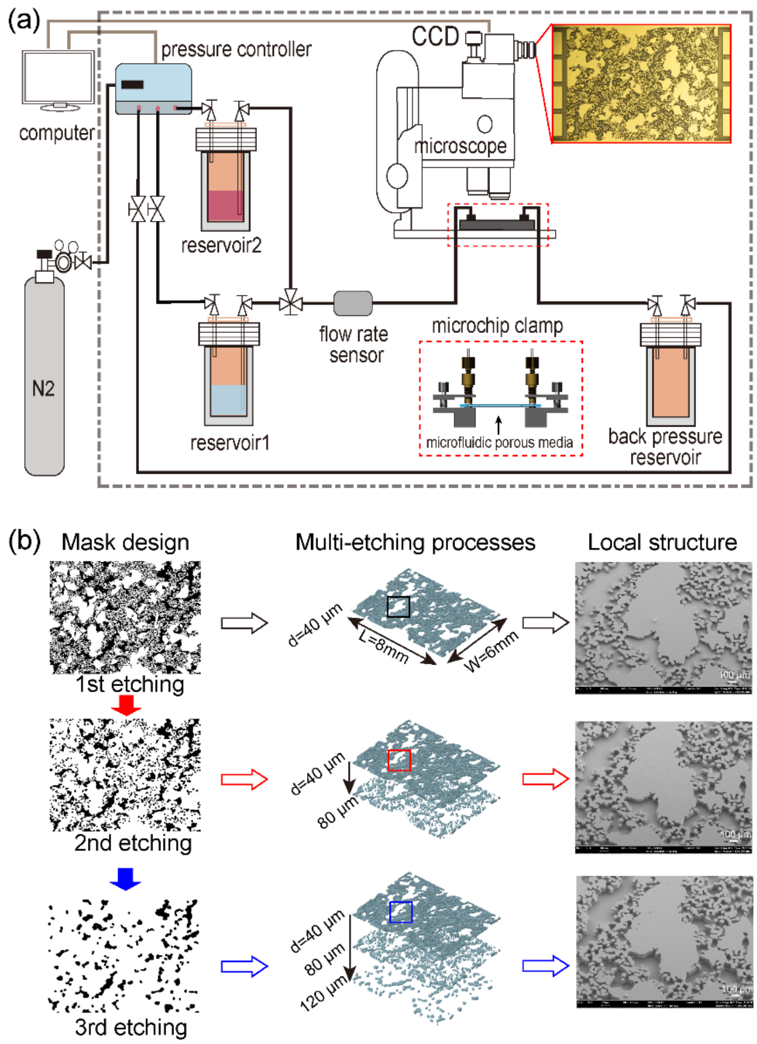

Figure S1. Microfluidic experimental setup and the fabrications of depth-variable microfluidic porous media. (a) Schematic diagram of the microfluidic-microscopy system. Reservoir 1 and Reservoir 2 are prepared for water and oil, respectively. For the water-air pair, Reservoir 2 should be closed. (b) The fabrication of the 2.5D microfluidic chips and corresponding 3D porous structures. The length (L), width (W), and depth (d) of the microfluidic porous media are 8 mm, 6 mm, and 40/80/120 μm, respectively. The black pattern represents the all area of 2D porous media, the blue pattern represents the middle and large pore area, and the red pattern represents the large pore area. Local structures of different depth-variable microfluidic chips are characterized by Scanning Electron Microscope (SEM).

Text S2: Image analysis for invading fluid saturation and Euler number

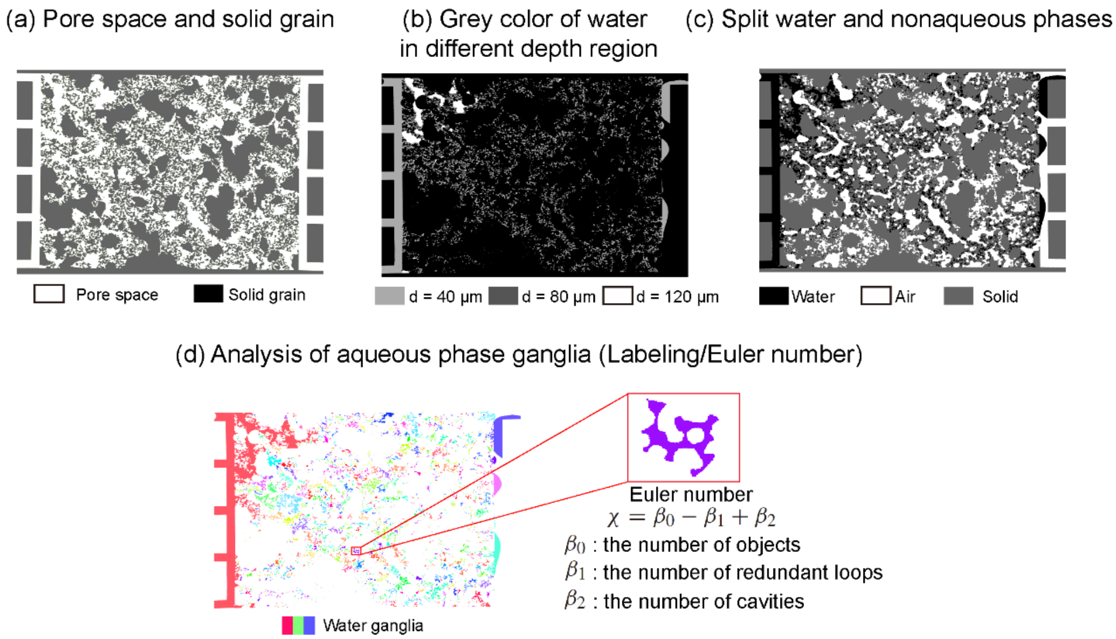

Figure S2. Quantitative image analysis based on fluorescence images of the displacement process. (a) All the pore space and solid grains in microfluidic porous media. (b) The grey color of the aqueous phase in different depth regions at the breakthrough stage. (c) Based on the image of the whole pore space and the space occupied by the water phase, the water phase and nonaqueous phase can be split. (d) Labeling each aqueous phase ganglia and calculating the Euler number.

Multiphase distributions and associated quantitative metrics were analyzed through a combination of ImageJ (an image analysis software) and the Image Processing Toolbox of MATLAB for a comprehensive assessment of porous media. Specialized programs were developed to scrutinize displacement in porous media. In the experimental image stacks, a Gauss filter was applied, and images were converted into binary format using the Otsu method, where invading fluid was represented in white, and defending fluid in black. Considering that only the invading phase or defending phase emits fluorescence signals, each binarized image was subtracted from the final fully water-saturated image or the initial fully oil-saturated image to identify the invaded phase at each time. Subsequently, noise removal and the ratio of white to black pixels were quantified to calculate different phases of saturation. These processes were executed using MATLAB. Finally, the number and volume fraction evolution of ganglia or clusters were determined to quantitatively evaluate displacement processes using the MorphoLibJ plugins of ImageJ. The Euler characteristic, linked to total curvature through the Gauss-Bonnet theorem, was employed as an average measure for fluid connectivity based on possible channels and disconnected regions. To quantify fluid distribution and displacement processes, the fluid topology was characterized using the Euler number ($\chi = \beta_0 - \beta_1 - \beta_2$, where β_0 is the number of objects, β_1 is the number of redundant loops, and β_2 is the number of cavities ignored in the microfluidic experiments). The entire image analysis process for calculating invading phase saturation and the Euler number is illustrated in Figure S2, where water is the invading fluid with fluorescence and air is the defending fluid.

Text S3: Introduction of direct numerical simulations

The numerical simulations of multiphase flow in microfluidic porous media were conducted utilizing the Volume of Fluid (VOF) method. The interFoam solver of the open-source library OpenFOAM was selected for its implementation of an algebraic VOF formulation. The governing equations for incompressible, two-phase, immiscible Newtonian fluids are as follows:

$$\begin{cases} \nabla \cdot \boldsymbol{u} = 0 \\ \dfrac{\partial(\rho \boldsymbol{u})}{\partial t} + \nabla \cdot (\rho \boldsymbol{u}\boldsymbol{u}) = -\nabla p + \nabla \cdot [\mu(\nabla \boldsymbol{u} + \nabla^T \boldsymbol{u})] + F_\gamma \end{cases} \tag{3.1}$$

where *t* is the time, $\boldsymbol{u}$ is the vector of the fluid velocity, p is the pressure, ρ is the density, μ is the dynamic viscosity, and they are the function of δ, defined as $\mu(\delta) = (1-\delta)\mu_d + \delta\mu_i$ and $\rho(\delta) = (1-\delta)\rho_d + \delta\rho_i$. $\delta = 1$ indicates the invading phase, $\delta = 0$ represents the defending phase, and $0 < \delta < 1$ denotes the presence of interfacial cells.

These equations are combined with a transport equation for the volume fraction δ

$$\frac{\partial \delta}{\partial t} + \nabla \cdot (\delta \boldsymbol{u}) = 0 \tag{3.2}$$

which can be regarded as a mass-conservation equation for the incompressible invading fluid and defending fluid separately.

According to the continuum surface force (CSF) model, the volumetric surface tension force F_σ is determined by (*Brackbill et al.*, 1992)

$$F_\gamma = \gamma \kappa \nabla \delta \tag{3.3}$$

where κ is the interface curvature, which can be obtained by $\kappa = -\nabla \cdot (\nabla \delta / |\nabla \delta|)$.

To limit the numerical diffusion of the interface and improve the accuracy of the interface capture, the additional convective term $\nabla \cdot [\delta(1-\delta)\boldsymbol{u}_r]$ is added into Eq. (2.2) which is only activated at the interface region ($0 < \delta < 1$).

$$\frac{\partial \delta}{\partial t} + \nabla \cdot (\delta \boldsymbol{u}) + \nabla \cdot [\delta(1-\delta)\boldsymbol{u}_r] = 0 \quad (3.4)$$

where $\boldsymbol{u}_r$ represents a suitable compression velocity carefully chosen to have no impact on the solution outside the interface region because of the factor $\delta(1-\delta)$. Through appropriate discretization and parameter selection, mass conservation of the phase fraction is ensured, yielding a solution that is both bounded and unbiased (*Ferrari and Lunati*, 2013). The term $\boldsymbol{u}_r = min[C_f|\boldsymbol{u}|, max(|\boldsymbol{u}|)]\boldsymbol{n}$ acts perpendicular to the interface, guided by the interface normal $\boldsymbol{n}$, where $max(|\boldsymbol{u}|)$ denotes the maximum velocity within the interface region, and C_f is a user-defined parameter governing compression strength. In our simulations, $C_f = 1$ is employed, ensuring conservative compression and a convergent numerical scheme: the compression term diminishes, and the interface thickness approaches zero (*Ferrari and Lunati*, 2013).

Within this numerical simulation framework, the influence of wettability on fluid flow is integrated by imposing an additional constraint on δ at the intersection between the interface and solid surface. This constraint is expressed as $\nabla\delta/|\nabla\delta||_{x\in wall} = \boldsymbol{n_s}\cos\theta + \boldsymbol{t_s}\sin\theta$, where θ represents the static contact angle of the invading fluid, $\boldsymbol{n_s}$ is the normal unit pointing into the solid and $\boldsymbol{t_s}$ is the unit tangent vector to the solid pointing into the invading phase. No-slip boundary conditions are applied for fluid-wall interactions. At the inlet and outlet of the porous medium, a rectangular buffer layer with a length of 40 μm is established. Initially, the invading phase fills the buffer layer at the inlet, while the defending phase occupies the remaining volumes. To ensure numerical stability, the time step Δt is automatically adjusted by the Courant number *Co*, where the maximum *Co* is set as 0.5. The simulations were conducted at the High-Performance Computing Center of Tsinghua University, China.

Text S4: Introduction of improved dynamic network model

The dynamic network model employs the two-pressure algorithm for multiphase distribution and pressure field evolution. In this model, each pore body contains two distinct phases, each assumed to have its pressure P_i^β in pore body *i* ($\beta = w$ for the wetting phase, $\beta = n$ for the non-wetting phase). The local capillary pressure in pore body *i*, denoted as P_i^c, following *Karsten E. Thompson* (2002), is $P_i^c = P_i^n - P_i^w = f(S_i^w)$, where S_i^w represents the wetting phase saturation, and P_i^n and P_i^w are the local pressure for the non-wetting and wetting phases, respectively.

For each fluid, a flow flux Q_{ij}^{β} is assigned in a throat *ij*, where the throat *ij* connects pore *i* and pore *j*. The total volumetric flux balance for pore *i* and the corresponding volumetric flux in pore throat *ij* is described as $\sum_{j=1}^{N_i}(Q_{ij}^{w} + Q_{ij}^{n}) = 0$ and $Q_{ij}^{\beta} = -K_{ij}^{\beta}\left(P_i^{\beta} - P_j^{\beta}\right)$, where N_i indicate the coordinate number of pore *i* in the pore system, and K_{ij}^{β} is the throat conductance as a function of geometry and fluid occupancy of pore throat *ij*. The volume balance in a pore body *i* for each fluid is expressed as $V_i \frac{\Delta S_i^{\beta}}{\Delta t} + \sum_{j=1}^{N_i} Q_{ij}^{\beta} = 0$, where ΔS_i^{β} is the saturation variation of fluid β in pore body *i* at a time interval Δt, V_i is the volume of the pore body *i*.

The entry capillary pressure for each pore throat in the imbibition process ($\theta < 90°$) is determined by solving nonlinear equations derived from the MS-P theory (*Mayer and Stowe*, 1965; *Princen*, 1969):

$$\begin{cases} A_n = (L_{nw} + L_{ns}\cos\theta)r = \begin{cases} A - 4r^2\left(\cos\theta\,(\cos\theta - \sin\theta) + \theta - \dfrac{\pi}{4}\right) & (\theta < 45°) \\ A & (\theta \geq 45°) \end{cases} \\ L_{ns} = \dfrac{R}{2G} - 8b \\ L_{nw} = 8r \cdot \arcsin\left(\dfrac{\sqrt{2}b}{2r}\right) \\ b = r \cdot max(0, \cos\theta - \sin\theta) \end{cases} \tag{4.1}$$

where G and A are the geometry factor and cross-section area of a pore-throat channel, the subscript *n* represents the non-wetting phase, L_{nw} and L_{ns} indicate the length of the immiscible interface and the nonwetting-wall interface, respectively. b is the meniscus-apex distance. θ is the contact angle on the wall. r is the curvature radius of the arc-menisci interface. R is the inscribed radius.

Building upon our direct simulation results, we have advanced the conventional dynamic pore-network model by incorporating the snap-off criterion in instances of strong imbibition and strong drainage. In situations where snap-off occurs during strong imbibition ($\theta < 45°$), it is imperative to account for both the critical capillary number condition and the geometrical condition of the pore-throat channel to discern pore-scale flow behavior. Conversely, for snap-off during strong drainage ($\theta > 135°$), only the geometrical condition of the pore-throat channel should be taken into consideration.

$$\begin{cases} P_{ij}^{c} \leq P_{c}^{snap-off} = \dfrac{\gamma}{R_{ij}}(\cos\theta - \sin\theta) \ \ (\theta < \ 45° \ or \ \theta > 135°) \\ Ca < Ca_c \quad (\theta < \ 45°) \end{cases} \tag{4.2}$$

where γ is the interface tension of the immiscible fluid, θ is the contact angle, and R_{ij} is the inscribed radius in each pore throat. The critical capillary number Ca_c is used to determine the domination of the main meniscus and corner flow. When the local capillary number is smaller than the critical value, the snap-off event will occur in the pore-throat obeying the geometry condition. The pore network of whole porous media is composed of a pore body with void volume and a pore throat with channel resistance.

The critical capillary number Ca_c has been proposed in our previous work (*Lei et al.*, 2023)

$$Ca_c = \sqrt{2/3}\, a(K\beta\tau)^{-1/2} \tag{4.3}$$

Here $\beta = C/[2\hat{g}_w(\cos\theta - \sin\theta)^4]$ represents the dimensionless flow resistance as a function of the contact angle. Other parameters are constant, such as *a*, which is a parameter introduced by the trial function, and the parameter *K*, which is calculated by a variational method (*Ransohoff and Radke*, 1988). For a tube with rectangular corners, *a* and *K* are 0.59 and 1.447, respectively. Here $\tau = 10^4$ is the dimensionless time for snap-off phenomena based on experimental observation (*Gauglitz and Radke*, 1986; *Gauglitz et al.*, 1987)

To overcome the constraints associated with a first-order approximation for the partial differential of the local capillary pressure, we utilized an automatic differentiation algorithm. This strategy enabled the implicit solution of the saturation equation, where the local capillary pressure is treated as a function of fluid saturation at the current timestep. Within this dynamic pore-network model, the pressure equation is explicitly solved, while the hydraulic conductance remains constant throughout a small-time interval.

Text S5: Benchmark of direct numerical simulations and dynamic network model

The multiphase flow dynamics under imbibition conditions in a rectangular tube are simulated with a direct numerical simulation framework by OpenFOAM and an improved dynamic network model, and the simulation results are compared with theoretical solutions to verify the accuracy of these numerical simulations. In this validation, the cross-section of the rectangular tube is 50 μm × 50 μm; the densities of the invading and defending phases are 1000 and 2.0

kg/m^3, respectively; the dynamic viscosities of the invading and defending phases are 1.0 and 0.02 $mPa \cdot s$, respectively, and the surface tension between the two fluids is 50 mN/m.

When the imbibition length becomes significantly extended, the impact of inertial forces can be disregarded, characterizing this phase as the viscous regime (*Fries and Dreyer*, 2008). In this regime, capillary and viscous forces primarily influence the dynamics, assuming the negligible contribution of gravitational forces. This condition is applicable, for instance, in imbibition within horizontal tubes or tubes with sufficiently small cross-sections. By assuming Hagen-Poiseuille flow in the tube, the displacement of the main meniscus can be accurately described using the well-established Washburn equation (*Washburn*, 1921).

$$x = \sqrt{\frac{\sigma \cos\theta\, R}{2\mu} t} \tag{4.1}$$

To validate the dynamics of the main meniscus flow under imbibition conditions, we imposed identical constant pressure boundary conditions for both the inlet and outlet. Initially, the defending phase occupies most of the tube, with a small quantity of the wetting liquid phase situated at the inlet, where a length of approximately 25 μm is for direct numerical simulations under mesh size $\Delta x = \Delta y = \Delta z = 1\ \mu m$ and a length of approximately 50 μm is for dynamic pore-network models under pore-network size $\Delta x = \Delta y = \Delta z = 50\ \mu m$. The relationships between imbibition length and time are presented in Figure S3 (a) for cases with contact angles θ=45°, 60° and 75°. Theoretical solutions were calculated based on Eq. (4.1). The simulation domain and corresponding multiphase distribution are presented in Figure S3 (b). It is important to note that the two-phase interface starts as a flat interface at the beginning of the direct numerical simulation, and extra time is required for this flat interface to attain an equilibrium shape. To mitigate the influence of this early period, the starting time of the direct numerical simulation is slightly adjusted by considering this extra time. As depicted in Figure S3, the results of direct numerical simulations and network models closely align with the theoretical solutions across various invading phase contact angles, affirming the precision of these numerical simulations in capturing the multiphase flow dynamics.

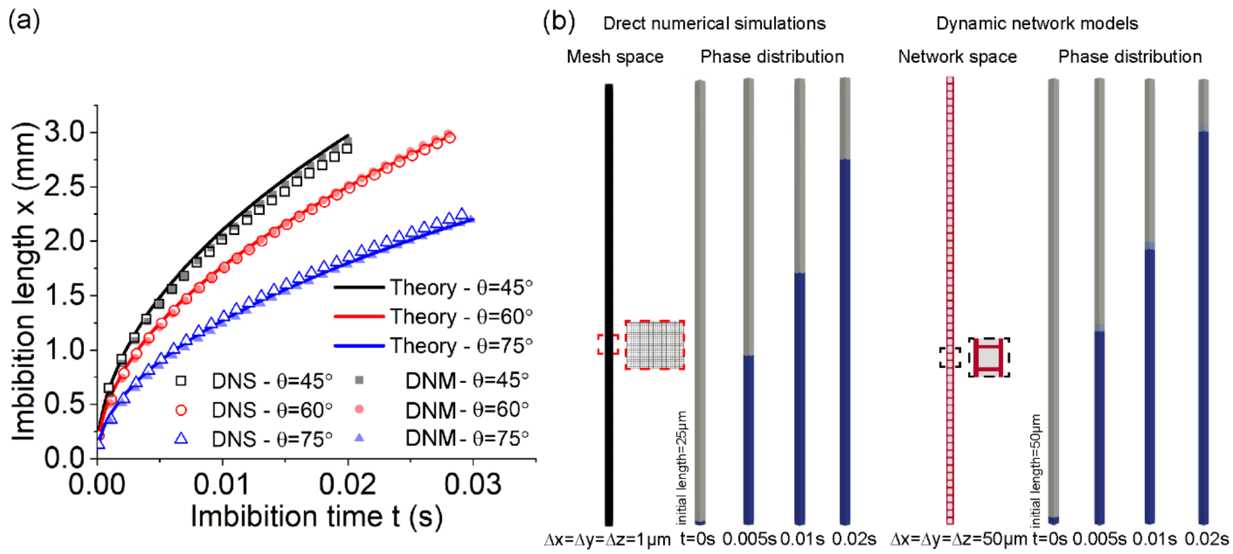

Figure S3. Comparison of theoretical results and numerical simulation results, including direct numerical simulations (DNS) and dynamic network models (DNM), about imbibition dynamics. (a) The curves of imbibition length of the main meniscus in the square tube are calculated by DNS and DNM, which can be described by the Washburn equation (*Washburn*, 1921). (b) The simulation domain of the square tube and corresponding phase distribution are calculated by DNS and DNM. The flow direction is from bottom to top.

Text S6: Validation of dynamic network models for multiphase flow in microfluidic porous media.

Figure S4 presents the validation of our DNM simulation for strong imbibition in 2D and 2.5D porous media and the comparison of our improved DNM and traditional DNM. Previous pore-scale models failed to capture the strong imbibition in porous media, this is because many capillary instabilities induced by the film or corner flow are ignored or incorrect considered in these DNM system (*He et al.*, 2021; *Joekar-Niasar and Majid Hassanizadeh*, 2011; *Joekar-Niasar et al.*, 2010; *Li et al.*, 2017; *Qin and van Brummelen*, 2019; *K. E Thompson*, 2002). Recent work introduced a capillary-driven criterion for the onset of corner flow, which states that this transition occurs when the local capillary pressure in upstreaming pore with main-meniscus flow exceeds the entry capillary pressure of the adjacent pore, as defined by the MS-P theory (*Qin and van Brummelen*, 2019). By integrating this criterion into the dynamic network model, we use this method as traditional DNM to demonstrate the advances of our improved DNM.

In Figure S4 (a-c), simulations based on the traditional DNM failed to capture the incomplete displacement pattern observed experimentally in 2D and 2.5D porous media. This limitation arises because the traditional DNM determines the onset of corner flow solely by comparing local capillary pressure and entry capillary pressure, without accounting for the influence of viscous forces on interfacial dynamics. Moreover, a quantification comparison of water saturation curve varied with time (Figure S4 d and e) proved the advances of our improved DNM. Compared with traditional DNM, our improved DNM can not only predict the displacement pattern qualitatively but also predict the saturation more accurately quantitatively.

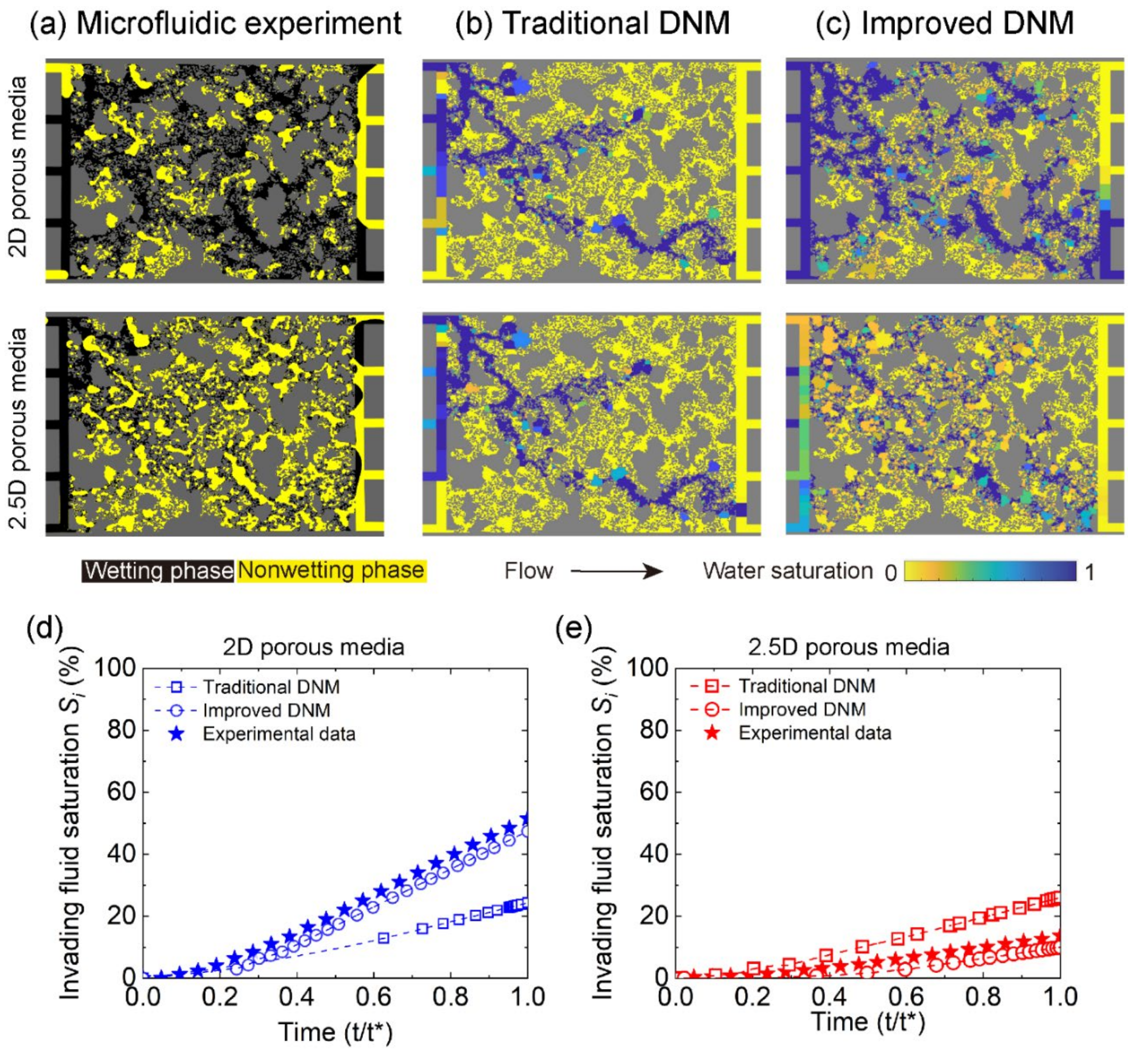

Figure S4. Comparison of multiphase displacement during strong imbibition in porous media. The spatial distribution of water and gas in 2D and 2.5 porous media at capillary number ($Ca=2.6\times10^{-6}$) from the (a) microfluidic experiments, (b) traditional DNM, and (c) our improved DNM; (d) and

(e) are the temporary variation of displacement efficiency under the corresponding multiphase flow conditions, t^* is the breakthrough time.

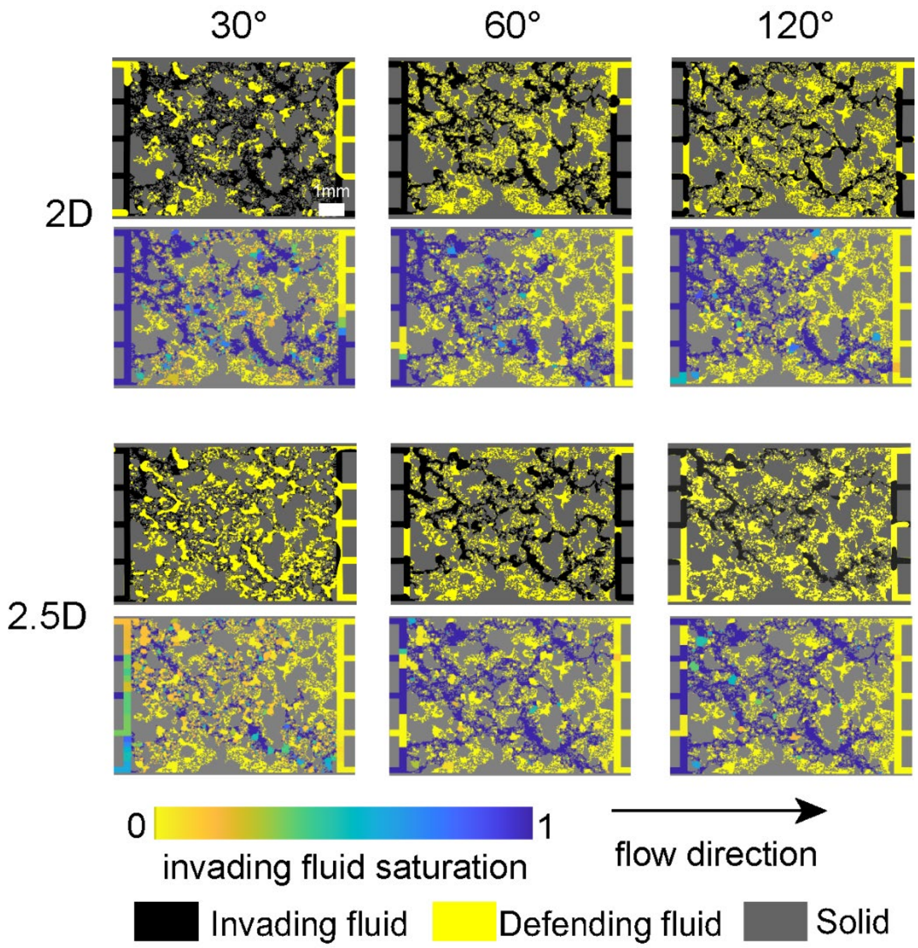

Figure S5. The comparison of DNM simulation results and microfluidic experimental results.

Text S6: Generality of wettability effect transition from 2D to 3D porous media.

In order to verify the universality of the wettability effect transition, we selected rocks with different reservoirs (Daqing Oilfield, Heilongjiang, China) but used the same method as in the main text. Consistent with the conclusion in the main text, when changing from a 2D porous medium to a 3D porous medium, the wettability effect gradually changes from monotonic to non-monotonic. Figure S6 (a) presents the representative phase distribution of the invading fluid at the breakthrough time in 2D, 2.5D, and 3D porous media with three different contact angles (θ = 20°, 60°, and 120°), which are simulated by improved DPNM. The invading saturation variation S_i of 2D, 2.5D and 3D porous media at the breakthrough stage are presented in Figure S6(b). The results for the 2D porous media (Figure S6 b) indicate a monotonic behavior for S_i with θ but the results for 2.5D and 3D porous media indicate a non-monotonic rule.

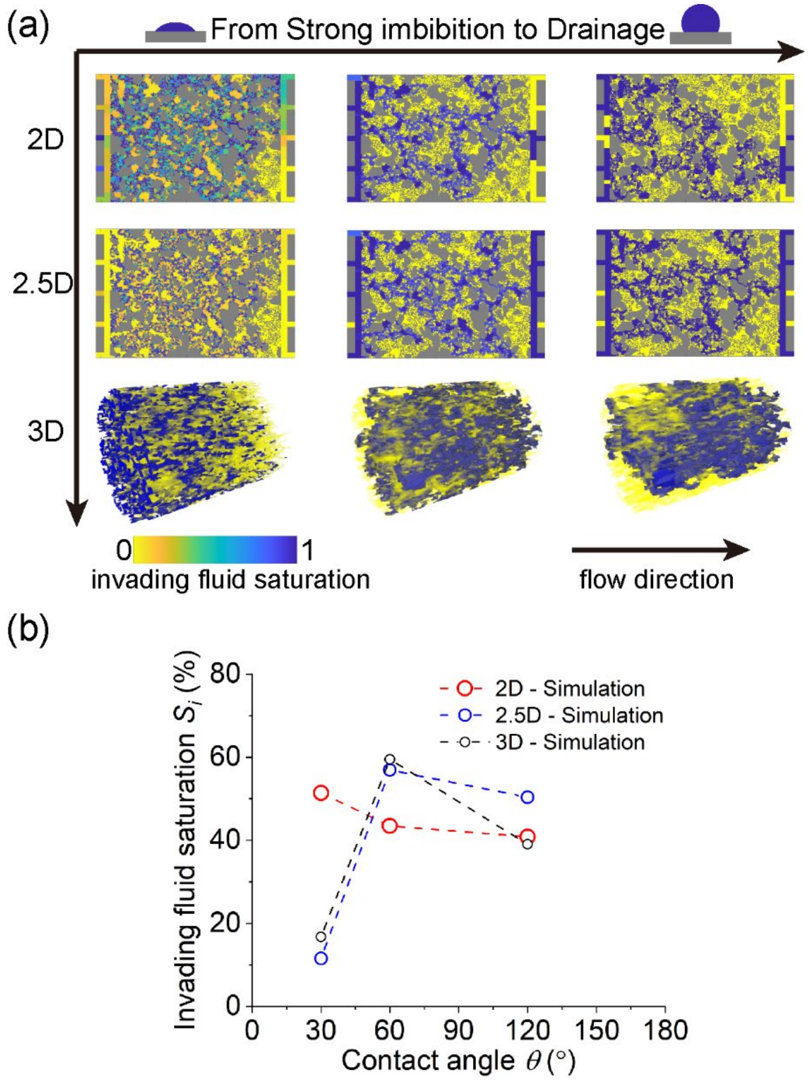

Figure S6. The transition from monotonic to non-monotonic wettability effects across 2D to 3D porous media. Here the 3D porous media is obtained from Daqing Oilfield, Heilongjiang, China and 2D and 2.5D porous media is regenerated based on this 3D porous media. (a) DNM simulation results about representative multiphase distribution in the 2D, 2.5D, and 3D porous media from strong imbibition to drainage conditions. (b) Variation in the invading fluid saturation at breakthrough versus the contact angle θ in 2D, 2.5D, and 3D porous media under θ = 30◦, 60◦, and 120◦.

References

Blunt, M. J. (2017), *Multiphase Flow in Permeable Media: A Pore-Scale Perspective*, Cambridge University Press, Cambridge.

Brackbill, J. U., D. B. Kothe, and C. Zemach (1992). A continuum method for modeling surface tension, *Journal of Computational Physics*, *100*(2), 335-354.

Chomsurin, C., and C. J. Werth (2003). Analysis of pore-scale nonaqueous phase liquid dissolution in etched silicon pore networks, *Water Resources Research*, *39*(9), 1265.

Ferrari, A., and I. Lunati (2013). Direct numerical simulations of interface dynamics to link capillary pressure and total surface energy, *Advances in Water Resources*, *57*, 19-31.

Fries, N., and M. Dreyer (2008). The transition from inertial to viscous flow in capillary rise, *Journal of Colloid and Interface Science*, *327*(1), 125-128.

Gauglitz, P. A., and C. J. Radke (1986), The Role of Wettability in the Breakup of Liquid Films Inside Constricted Capillaries, in *AIChE Symposium Series, 252, Thin Liquid Film Phenomena, ed. W.B. Krantz, D.T. Wasan, and R.K. Jain*, edited.

Gauglitz, P. A., C. M. St. Laurent, and C. J. Radkle (1987). An Experimental Investigation of Gas-Bubble Breakup in Constricted Square Capillaries, *Journal of Petroleum Technology*, *39*(09), 1137-1146.

He, M., Y. Zhou, K. Wu, Y. Hu, D. Feng, T. Zhang, Q. Liu, and X. Li (2021). Pore network modeling of thin water film and its influence on relative permeability curves in tight formations, *Fuel*, *289*, 119828.

Joekar-Niasar, V., and S. Majid Hassanizadeh (2011). Effect of fluids properties on non-equilibrium capillarity effects: Dynamic pore-network modeling, *International Journal of Multiphase Flow*, *37*, 198-214.

Joekar-Niasar, V., M. Prodanović, D. Wildenschild, and S. M. Hassanizadeh (2010). Network model investigation of interfacial area, capillary pressure and saturation relationships in granular porous media, *Water Resources Research*, *46*(6).

Lei, W., X. Lu, W. Gong, and M. Wang (2023). Triggering interfacial instabilities during forced imbibition by adjusting the aspect ratio in depth-variable microfluidic porous media, *Proceedings of the National Academy of Sciences*, *120*(50), e2310584120.

Lei, W., W. Gong, X. Lu, and M. Wang (2024). Fluid entrapment during forced imbibition in a multidepth microfluidic chip with complex porous geometry, *Journal of Fluid Mechanics*, *987*, A3.

Lei, W., T. Liu, C. Xie, H. Yang, T. Wu, and M. Wang (2020). Enhanced oil recovery mechanism and recovery performance of micro-gel particle suspensions by microfluidic experiments, *Energy Science & Engineering*, *8*(4), 986-998.

Li, J., S. R. McDougall, and K. S. Sorbie (2017). Dynamic pore-scale network model (PNM) of water imbibition in porous media, *Advances in Water Resources*, *107*, 191-211.

Mayer, R. P., and R. A. Stowe (1965). Mercury porosimetry—breakthrough pressure for penetration between packed spheres, *J Colloid Sci*, *20*(8), 893-911.

Princen, H. M. (1969). Capillary phenomena in assemblies of parallel cylinders: I. Capillary rise between two cylinders, *Journal of Colloid and Interface Science*, *30*(1), 69-75.

Qin, C.-Z., and H. van Brummelen (2019). A dynamic pore-network model for spontaneous imbibition in porous media, *Advances in Water Resources*, *133*, 103420.

Ransohoff, T. C., and C. J. Radke (1988). Laminar flow of a wetting liquid along the corners of a predominantly gas-occupied noncircular pore, *Journal of Colloid and Interface Science*, *121*(2), 392-401.

Thompson, K. E. (2002). Pore-scale modeling of fluid transport in disordered fibrous materials, *AIChE Journal*, *48*(7), 1369-1389.
Thompson, K. E. (2002). Pore-Scale Modeling of Fluid Transport in Disordered Fibrous Materials, *AIChE Journal*, *48*(7), 1369-1389.
Wang, M., J. Wang, N. Pan, and S. Chen (2007). Mesoscopic predictions of the effective thermal conductivity for microscale random porous media, *Physical Review E*, *75*(3), 036702.
Washburn, E. W. (1921). The Dynamics of Capillary Flow, *Physical Review*, *17*(3), 273-283.